Summaries of the Fourth Annual JPL Airborne Geoscience Workshop October 25–29, 1993

Volume 2. TIMS Workshop

Vincent J. Realmuto
Editor

October 25, 1993

NASA

ABSTRACT

This publication contains the summaries for the Fourth Annual JPL Airborne Geoscience Workshop, held in Washington, D. C. on October 25–29, 1993. The main workshop is divided into three smaller workshops as follows:

- The Airborne Visible/Infrared Imaging Spectrometer (AVIRIS) workshop, on October 25–26. The summaries for this workshop appear in Volume 1.

- The Thermal Infrared Multispectral Scanner (TIMS) workshop, on October 27. The summaries for this workshop appear in Volume 2.

- The Airborne Synthetic Aperture Radar (AIRSAR) workshop, on October 28–29. The summaries for this workshop appear in Volume 3.

CONTENTS

Volume 1: AVIRIS Workshop

Volume 3: AIRSAR Workshop

Estimation of spectral emissivity in the thermal infrared

David Kryskowski and J. R. Maxwell

Environmental Research Institute of Michigan
3300 Plymouth Rd., Ann Arbor, Michigan   48105

1. INTRODUCTION

A number of algorithms are available in the literature that attempt to remove most of the effects of temperature from thermal multispectral data where the final goal is to extract emissivity differences. Early approaches include adjacent spectral band ratioing, broad band radiance normalization and the use of one band where emissivities are generally high (e.g., 11 to 12 μm) to determine the temperature (Salisbury, 1992). More recent work (Salisbury, 1992) has produced two techniques that use data averaging to extract temperature to leave a quantity related to emissivity changes. These two techniques (Thermal Log Residuals and Alpha Residuals) have been investigated and compared and appear to provide reasonable results.

The analysis presented in this paper develops a thermal IR multispectral temperature/emissivity estimation procedure based on formal estimation theory, Gaussian statistics, and a stochastic radiance signal model including the effects of both temperature and emissivity. The importance of this work is that this is an optimal estimation procedure which will provide minimum variance estimates of temperature and emissivity changes directly.

Section 2 discusses optimal linear spectral emissivity estimation and Section 3 is a summary.

2. OPTIMAL LINEAR SPECTRAL EMISSIVITY ESTIMATION

A stochastic model for the spectral radiance in the thermal IR using the Planck equation ignoring reflection and atmospheric contributions is:

$$L(\lambda, \overline{T}) = \frac{c_1}{\pi \lambda^5} \frac{1}{e^{c_2/\lambda \overline{T}} - 1} \left\{ \overline{\epsilon}(\lambda) + \Delta\epsilon(\lambda) + \frac{c_2 \overline{\epsilon}(\lambda) \Delta T}{\lambda \overline{T}^2} \right\} \quad (1)$$

c_1 First Radiation Constant
c_2 Second Radiation Constant
$\overline{T}$ Average background temperature in region
$\overline{\epsilon}(\lambda)$ Average background emissivity in region
λ Wavelength
ΔT Change in background temperature (a zero mean random variable)
$\Delta\epsilon(\lambda)$ Change in background emissivity (a zero mean random process)

The term in braces in Equation 1 is the apparent emissivity, $\epsilon^{app}(\lambda)$. The model assumes samples are independent and identically distributed spatially. From Equation 1   it is clear that changes in temperature affect all wavelengths uniformly. Thus ΔT can be considered as a random process of rank

one with respect to wavelength. In a generalized sense it is also considered to be narrowband since all of the variation induced by temperature will fall along a single direction with a properly chosen expansion basis for the spectral radiance. The covariance of the apparent emissivity can be computed assuming that temperature and emissivity are independent as :

$$K_{eapp}(\lambda, \eta) = K_{e}(\lambda, \eta) + \frac{c_2^2 \, \overline{\epsilon}(\lambda) \, \overline{\epsilon}(\eta)}{\lambda \eta \, \overline{T}^4} \sigma_{\Delta T}^2 \qquad (2)$$

The second term on the right hand side of Equation 2 is (to within the temperature variance) known. Moreover in an absolute sense the second term more often is the dominant one (thermal IR phenomenology tells us this, especially in the daytime) since it is the one dependent on temperature. The first term on the right hand side of the equation is more difficult to specify. In order to describe it for a certain class of material an ensemble of measurements is needed for that class. Since only a very limited number of measurements exist for spectral emissivity in the thermal IR, a description of the first term for an arbitrary class is not available. In this development it will be assumed that the first term is stationary white. That is:

$$K_{e}(\lambda, \eta) = \frac{N_e}{2} \delta(\lambda - \eta) \qquad (3)$$

This assumption is very appealing for large regions because large regions usually contain many different classes of materials and it is reasonable to assume the second order statistics of the ensemble are white.

2.1 Cancellation of Narrow Band Interference (Temperature)

What follows here is a procedure for separating temperature and emissivity. What motivates the procedure is the observation that emissivity and temperature cannot be separated from a single multispectral measurement but a statistically based procedure can provide separation with acceptable error. Again writing Equation 1 but including sensor noise $w(\lambda)$:

$$L(\lambda, \overline{T}) = L^{BB}(\lambda, \overline{T}) \left\{ \overline{\epsilon}(\lambda) + \Delta\epsilon(\lambda) + \frac{c_2 \overline{\epsilon}(\lambda) \, \Delta T}{\lambda \overline{T}^2} \right\} + w(\lambda) \qquad (4)$$

Since the means are assumed to be known or well estimated from the data, the mean radiance can be subtracted off along with a division by the blackbody function to obtain the following equation for observed variation in apparent emissivity:

$$\Delta\epsilon^{app}(\lambda) = \Delta\epsilon(\lambda) + \frac{c_2 \overline{\epsilon}(\lambda) \, \Delta T}{\lambda \overline{T}^2} + w'(\lambda) \qquad (5)$$

The quantity $\Delta\epsilon(\lambda)$ contains the relative emissivity behavior and it is this component that needs to be estimated. To estimate a realization of the random process $\Delta\epsilon(\lambda)$, the covariance of the apparent

emissivity is needed. The covariance of Equation 5 can be written as

$$K_{\epsilon app}(\lambda, \eta) \; = \; K_\epsilon(\lambda, \eta) \; + \; \frac{c_2^2 \, \overline{\epsilon}(\lambda) \, \overline{\epsilon}(\eta)}{\lambda \eta \, \overline{T}^4} \sigma_{\Delta T}^2 \; + \; \frac{N_o}{2} \delta(\lambda - \eta) \qquad (6)$$

Here $N_o/2$ is the strength of the white sensor noise. It is recognized that the sensor noise term will not be stationary white due to the division by the Planck function. This will be ignored because modern sensors are generally clutter limited not noise limited, so a stationary assumption should introduce very little error. The second and third term of Equation 6 will be considered as known. Since it is assumed that the emissivity covariance is stationary white, the form of the apparent emissivity covariance is:

$$K_{\epsilon app}(\lambda, \eta) \; = \; \frac{c_2^2 \, \overline{\epsilon}(\lambda) \, \overline{\epsilon}(\eta)}{\lambda \eta \, \overline{T}^4} \sigma_{\Delta T}^2 \; + \; \frac{N_o + N_\epsilon}{2} \delta(\lambda - \eta) \qquad (7)$$

The estimation filter is required to be linear but not necessarily shift invariant with respect to wavelength. This implies that not only stationary but nonstationary random processes can be estimated as well. In fact the stochastic description of the temperature behavior clearly indicates that it is nonwhite and nonstationary due to its non Toeplitz form:

$$K_{\Delta T}(\lambda, \eta) \; = \; \frac{c_2^2 \, \overline{\epsilon}(\lambda) \, \overline{\epsilon}(\eta)}{\lambda \eta \, \overline{T}^4} \sigma_{\Delta T}^2 \qquad (8)$$

The optimal linear filter for estimating the temperature driven part of $\epsilon^{app}(\lambda)$, $h_o(\lambda,\eta)$, is obtained from the following integral equation (Van Trees, 1968,1971):

$$\frac{(N_o + N_\epsilon)}{2} h_o(\lambda, \eta) \; + \; \int_{\lambda_i}^{\lambda_f} h_o(\lambda, x) \, K_{\Delta T}(x, \eta) \, dx \; = \; K_{\Delta T}(\lambda, \eta) \quad \lambda_i < \eta, \quad \lambda < \lambda_f \qquad (9)$$

Equations of this form are fundamental to all linear signal processing. A series solution to this equation is obtained by using the eigenfunctions and eigenvalues of $K_{\Delta T}(\lambda,\eta)$. Since the temperature driven term is rank one there is only one eigenfunction and eigenvalue and the optimal filter can be written as

$$h_o(\lambda, \eta) \; = \; \frac{\dfrac{c_2^2 \sigma_{\Delta T}^2}{\overline{T}^4}}{\dfrac{(N_o + N_\epsilon)}{2} + \dfrac{c_2^2 \sigma_{\Delta T}^2}{\overline{T}^4} \displaystyle\int_{\lambda_i}^{\lambda_f} \dfrac{\overline{\epsilon}^2(x)}{x^2} \, dx} \; \frac{\overline{\epsilon}(\lambda)}{\lambda} \, \frac{\overline{\epsilon}(\eta)}{\eta} \qquad (10)$$

This filter, when applied to the stochastic portion of the signal, will produce an estimate of the correlated component driven by temperature. The filter projects the observables onto the temperature direction defined by $\overline{\epsilon}(\lambda) / \lambda$. To produce an estimate of the stochastic portion of the emissivity, $\Delta \epsilon(\lambda)$, the weighted projection is subtracted from the observations. The weighting is important because

if all the energy were to be taken out in the temperature direction the "space" spanned by the emissivity would be dimensionally too small providing poorer estimates. To make the emissivity estimation equation simple in form the following are defined:

$$\Phi_1(\lambda) = \frac{\overline{\epsilon}(\lambda)}{\lambda}\left[\int_{\lambda_i}^{\lambda_f} \frac{\overline{\epsilon}^2(x)}{x^2}\right]^{-1/2} \tag{11}$$

$$\zeta_1 = \frac{c_2^2\, \sigma_{\Delta T}^2}{\overline{T}^4}\int_{\lambda_i}^{\lambda_f} \frac{\overline{\epsilon}^2(x)}{x^2} \tag{12}$$

$$\sigma^2 = \frac{N_0 + N_\epsilon}{2} \tag{13}$$

The optimal estimate of emissivity becomes

$$\Delta\hat{\epsilon}(\lambda) = \Delta\epsilon^{app}(\lambda) - \frac{\zeta_1}{\sigma^2 + \zeta_1}\left\{\int_{\lambda_i}^{\lambda_f}\Delta\epsilon^{app}(\eta)\, \Phi_1(\eta)\, d\eta\right\}\Phi_1(\lambda) \tag{14}$$

Equation 14 is the best linear minimum mean square estimate of the spectral emissivity which is the spectral apparent emissivity less the contribution from temperature variation.

3. SUMMARY

Temperature variations cause variations in the multispectral data that are highly correlated between spectral bands. Although many phenomenology based techniques have been developed to remove the variations due to temperature from the data, it has been shown in this paper that a formal development of the optimal estimator includes a temperature projection filter to remove the correlated variations due temperature leaving a direct estimate of emissivity changes.

4. REFERENCES

Salisbury, J.W., ed., *Remote Sensing of Environment: Special Issue on Emissivity and Temperature Separation*, Vol. 42, No. 2, November 1992.

Van Trees, H. L., *Detection, Estimation, and Modulation Theory*, Part I, Wiley, 1968.

Van Trees, H. L., *Detection, Estimation, and Modulation Theory*, Part III, Wiley, 1971.

4

THE DIFFERENCE BETWEEN LABORATORY AND IN-SITU PIXEL-AVERAGED EMISSIVITY: THE EFFECTS ON TEMPERATURE-EMISSIVITY SEPARATION

Tsuneo Matsunaga

Geophysics Department, Geological Survey of Japan
1-1-3, Higashi, Tsukuba, Ibaraki, 305, Japan

1.   INTRODUCTION

Advanced Spaceborne Thermal Emission and Reflection Radiometer(ASTER) is a Japanese future imaging sensor which has five channels in thermal infrared(TIR) region. To extract spectral emissivity information from ASTER and/or TIMS data, various temperature-emissivity(T-E) separation methods have been developed to date. Most of them require assumptions on surface emissivity, in which emissivity measured in a laboratory is often used instead of in-situ pixel-averaged emissivity. But if these two *emissivities* are different, accuracies of separated emissivity and surface temperature are reduced.

In this study, the difference between laboratory and in-situ pixel-averaged emissivity and its effect on T-E separation are discussed. TIMS data of an area containing both rocks and vegetation were also processed to retrieve emissivity spectra using two T-E separation methods.

2.   THE DIFFERENCE BETWEEN LABORATORY AND IN-SITU PIXEL-AVERAGED EMISSIVITY OF LAND SURFACE

The difference between laboratory and in-situ pixel-averaged emissivity has several causes. A pixel generally contains different materials of different temperatures. Since a pure isothermal sample is usually measured in a laboratory, laboratory emissivity may differ from pixel-averaged emissivity(heterogeneity effect).

Due to less-than-unity emissivity of land surface, incident thermal radiation to the surface is partially reflected and observed by a sensor. Incident radiation consists of downwelling radiance from the atmosphere including clouds and thermal radiation from the surrounding. In addition to reflection, the surface roughness causes scattering of thermal emission from the surface itself. Thus, apparent emissivity is expected to be higher than laboratory emissivity because of these scattering/reflection effect.

3.   TEMPERATURE-EMISSIVITY SEPARATION METHODS

In this study, Emissivity Spectrum Normalization(ESN: *Realmuto*, 1990) and Mean-Maximum Difference(MMD: *Matsunaga*, 1993a, b) methods were considered. The MMD method is based on a relationship between the mean and the spectral variation of emissivity of terrestrial materials in TIR region. Similar methods have been developed by *Kealy and Gabell* [1990], *Stoll* [1991] and *Hook* [personal communication]. In the MMD method, the relationship between the mean(M) and the difference between the maximum and the minimum(Maximum Difference: MD) of emissivity for TIMS six channels is assumed to be linear. MD corresponds to spectral contrast or variation. Surface temperature and spectral emissivity can be separated based on this assumption. Fig. 1 shows M-MD relationship for various earth's surface materials. Volcanic rocks have high contrast and low mean of spectral emissivity. On the contrary, spectra of water surface and vegetation are very flat and close to unity. This relationship can be approximated to linear, though the distribution is somewhat scattered.

4.   EVALUATION OF EFFECTS OF SURFACE HETEROGENEITY AND SCATTERING/REFLECTION BY SIMPLE SIMULATIONS

4.1.   Surface Heterogeneity

Pixel-averaged emissivity of an isothermal pixel comprised of two materials
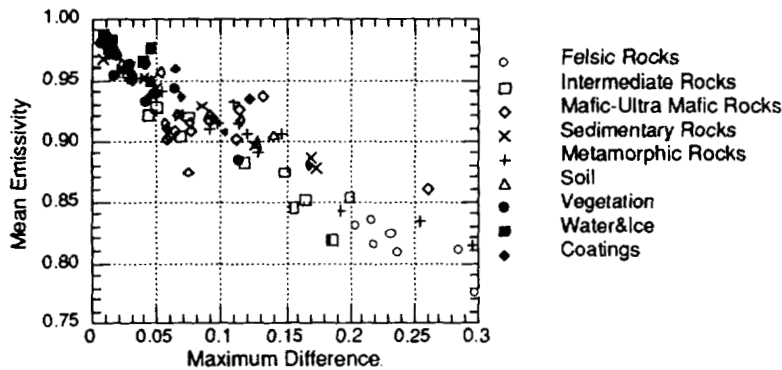
Fig. 1 Mean-maximum difference relationship for various terrestrial materials.
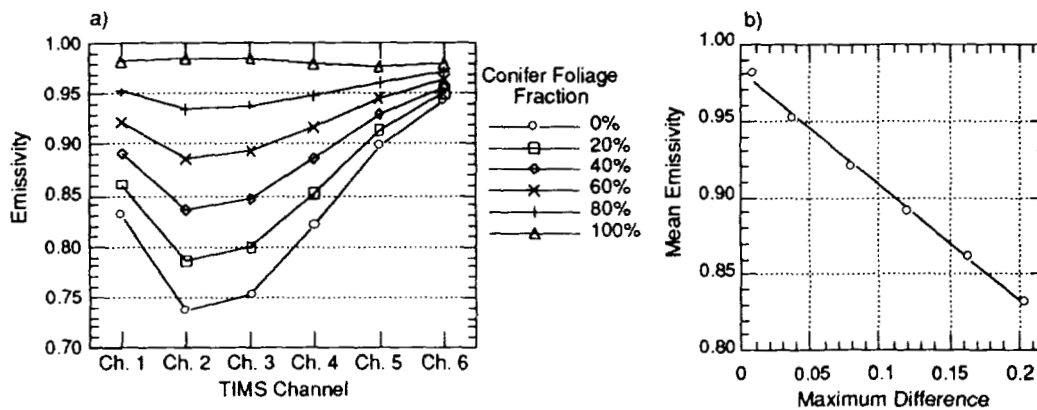
Fig. 2 Pixel-averaged emissivity spectra(a) and M-MD relationship(b) for varying areal fraction of conifer foliage.

having different spectral emissivity was calculated to evaluate the heterogeneity effect on spectral emissivity. Rhyolite and conifer foliage were chosen as the materials because volcanic rocks and vegetation generally have very different emissivity spectra. Simulated pixel-averaged emissivity spectra corresponding to varying conifer foliage area fraction are shown in Fig. 2a. Maximum emissivity increases according to the fraction. Therefore, assuming constant maximum emissivity in the ESN method causes errors if vegetation fraction in a pixel varies within a scene. Fig. 2b shows M-MD relationship for this case. Spectra of mixed pixels almost satisfy the linear relationship determined from pure rhyolite and conifer foliage spectra.

4.2. Surface Scattering/Reflection of Thermal Radiation

Because detailed calculation of scattering/reflection effects at land surface is difficult, single reflection effect was considered in case of the geometry shown in Fig. 3. The surface was illuminated by thermal emission from the surrounding wall. Both of them were assumed to be isothermal and isotropic reflectors/emitters with same emissivity as rhyolite and have same temperature. Long-wave sky radiation was ignored. Simulated emissivity spectra were shown in Fig. 4a for varying angle θ. As θ decreases, spectral contrast decreases and emissivity values increases. Thus, neglecting the scattering/reflection effect on surface emissivity results in overestimation of surface temperature. M-MD relationship was linear for varying θ(Fig. 4b).

These simulations show that the effects of surface heterogeneity and scattering/reflection can change in-situ pixel-averaged emissivity from the value measured in a laboratory. The robustness of the assumption used in the MMD method is also shown.

5. EXTRACTION OF EMISSIVITY SPECTRA FROM TIMS DATA

5.1. Acquisition and Atmospheric Correction of TIMS Data

6
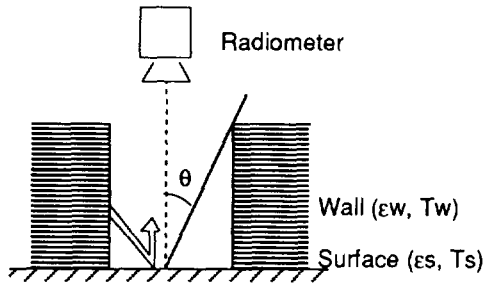
Fig. 3 A simple model for the simulation of scattering/reflection effect at the surface.
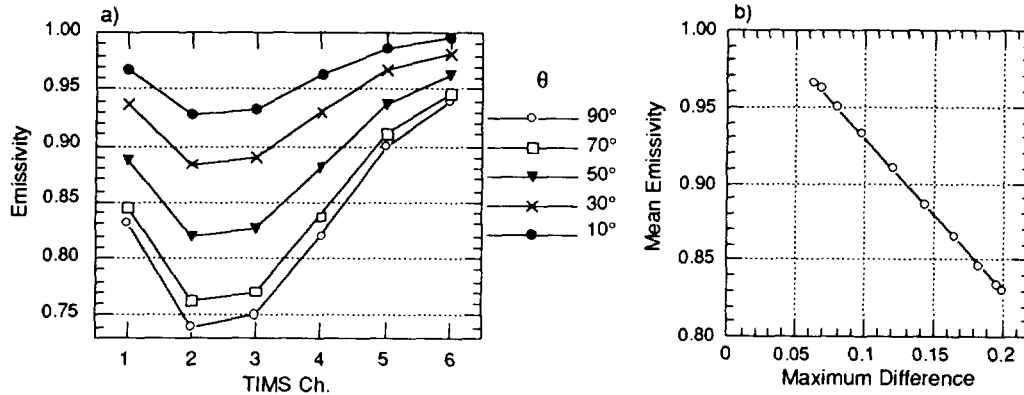
Fig. 4 Apparent emissivity spectra(a) and M-MD relationship(b) including single reflection effect. The surface and the wall were assumed to have rhyolite emissivity spectrum and same temperature.

TIMS data used in this study were acquired over Mono Lake/Mammoth Lakes area, California, on October 16, 1991. This area is located at the east flank of the Sierra Nevada. Flight altitude, spatial and temperature resolutions were about 7.5 km ASL, 13 m, and 0.25 - 0.30°C, respectively.

Atmospheric transmittance and upwelling radiance for each TIMS channel were preliminarily calculated using LOWTRAN7 with data from a radiosonde launched at the time of the overflight. Though lake surface brightness temperatures for TIMS Ch. 5 and 6 were same after LOWTRAN-based atmospheric correction, temperature for Ch. 1, 2, and 4 were higher than Ch. 5 and 6(Fig. 5) This discrepancy was also found at dark-grayish sand beach with a little grass. In this study, atmospheric transmittance and upwelling radiance calculated from TIMS data of the lake surface and the beach were used. For this calculation, it was assumed that these two sites were blackbody and brightness temperatures in Ch. 5 after LOWTRAN-based atmospheric correction were true surface temperatures.

5.2.   Temperature-Emissivity Separation

The ESN and the MMD methods were applied to atmospherically corrected TIMS radiance data to retrieve surface emissivity spectra. Fig. 6 shows retrieved spectra for the transect from a coniferous forest to rhyolite-dominated field at the flank of Crater Mountain. Both methods could obtain emissivity troughs corresponding to SiO_2 content for rhyolite, and flat spectra for forest. In addition, the MMD method could show higher emissivity values for the forest than for rhyolite and transitional spectra from forest to rhyolite(Point 57 and 58).

6.   CONCLUSION

Simple simulations showed that in-situ pixel-averaged emissivity may differ from emissivity measured in a laboratory due to the effects of surface heterogeneity and scattering/reflection. It was also shown that T-E separation methods based on the relationship between the mean and the variation of spectral emissivity are relatively robust to these effects. It must be noted, however, that retrieved emissivity by these methods is apparent and still including scattering/reflection contribution.

ACKNOWLEDGEMENTS
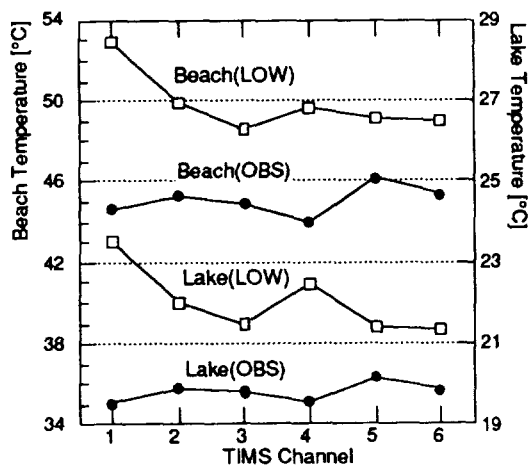
Fig. 5 TIMS brightness temperature of
Mono Lake and the beach.
OBS: observed temperature
LOW: after LOWTRAN7-based
atmospheric correction.
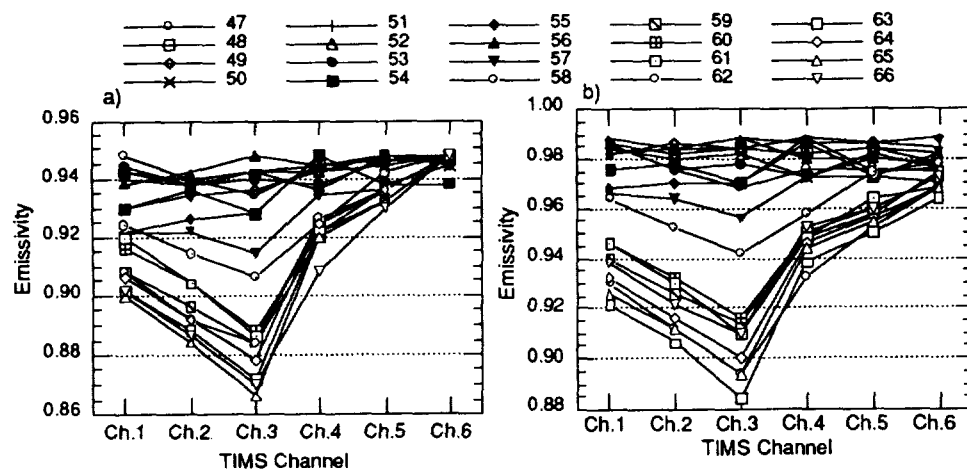
Fig. 6 Retrieved emissivity spectra from TIMS data for the transect
from coniferous forest(47) to rhyolite field(66). a) ESN method, b) MMD method.

sity of Tokyo, Japan, for providing emissivity data of terrestrial materials integrated over
TIMS response functions. Original emissivity spectra are described in *Salisbury et
al.*[1988] and *Salisbury et al.*[1992]. The author is also grateful to personnels of JPL,
DRI, University of Nevada System, and JAPEX Geoscience Institute who cooperated in
the acquisition of TIMS data and field works.

REFERENCES

Kealy, P. S., and A. R. Gabell, 1990. " Estimation of Emissivity and Temperature Using
   Alpha Coefficients", *Proc. of the Second TIMS Workshop*, JPL Publ. 90-55, pp. 11-16.
Matsunaga, T., 1993a, "An Emissivity-Temperature Separation Technique Based on an
   Empirical Relationship between Mean and Range of Spectral Emissivity", *Proc. of the
   14th Japanese Conference of Remote Sensing*, pp. 47-48(in Japanese).
Matsunaga, T., 1993b, "Emissivity Spectra Derived from TIMS Data Acquired over a
   Partially Vegetated Area", *Proc. of 1993 International Geoscience and Remote Sensing
   Symposium(IGARSS '93)*(to be published).
Realmuto, V. J., 1990, "Separating the Effects of Temperature and Emissivity: Emissivity
   Spectrum Normalization", *Proc. of the Second TIMS Workshop*, JPL Publ. 90-55, pp.
   31-35.
Salisbury, J. W., L. S. Walter, and D. D'Aria, 1988, "Midinfrared(2.5 to 13.5μm) Spectra
   of Igneous Rocks", USGS Open File Report 88-686, Reston, VA, 126pp.
Salisbury, J. W., and D. M. D'Aria, 1992, "Emissivity of Terrestrial Materials in the 8-14
   μm Atmospheric Window", Remote Sensing of Environment, vol. 42, pp. 83-106.
Stoll, M., 1991, "Land Surface Temperature and Emissivity Retrieval from Passive
   Remote Sensing Measurements", *Proc. of the Third TIMS Workshop*, JPL Publ. 91-29,
   pp. 10-19.

Mineralogic Variability of the Kelso Dunes, Mojave Desert, California Derived From Thermal Infrared Multispectral Scanner (TIMS) Data

Michael S. Ramsey[1], Douglas A. Howard[1],
Philip R. Christensen[1] and Nicholas Lancaster[2]

[1]Department of Geology
Arizona State University
Tempe, Arizona 85287-1404

[2]Desert Research Institute
7010 Dandini Blvd.
Reno, Nevada 89512

1. Introduction

Mineral identification and mapping of alluvial material using thermal infrared (TIR) remote sensing is extremely useful for tracking sediment transport, assessing the degree of weathering and locating sediment sources. As a result of the linear relation between a mineral's percentage in a given area (image pixel) and the depth of its diagnostic spectral features, TIR spectra can be deconvolved in order to ascertain mineralogic percentages (Ramsey and Christensen, 1992; Gillespie, et al., 1990). Typical complications such as vegetation, particle size and thermal shadowing (Ramsey and Christensen, 1993) are minimized upon examination of dunes. Actively saltating dunes contain little to no vegetation, are very well sorted and lack the thermal shadows that arise from rocky terrain. The primary focus of this work was to use the Kelso Dunes as a test location for an accuracy analysis of temperature/emissivity separation and linear unmixing algorithms. Accurate determination of ground temperature and component discrimination will become key products of future ASTER data.

A decorrelation stretch of the TIMS image showed clear color variations within the active dunes. Samples collected from these color units were analyzed for mineralogy, grain size, and separated into endmembers. This analysis not only reveled that the dunes contained significant mineralogic variation (Fig. 1), but were more immature (low quartz percentage) then previously reported (Sharp, 1966; Yeend, et al., 1984). Unmixing of the TIMS data using the primary mineral endmembers produced unique variations within the dunes and may indicate near, rather than far, source locales for the dunes.

The Kelso Dunes lie in the eastern Mojave Desert, California approximately 95 km west of the Colorado River. The primary dune field is contained within a topographic basin bounded by the Providence, Granite, Bristol and Kelso Mountains to the east, south, west and north, respectively. The dune field rests upon the alluvial fans which extend from the Providence and Granite Mountains, with the active region marked by three northeast trending linear ridges. Although active, the dunes appear to lie at an opposing regional wind boundary which produces little net movement of the crests (Sharp, 1966). Previous studies have estimated the dunes range from 70% (Sharp, 1966) to 90% (Paisley, et al., 1991) quartz mainly derived from a source 40 km to the west. The dune field is assumed to have formed in a much more arid climate than present, with the age of the deposit estimated at greater than 100,000 years (Yeend, et al., 1984).
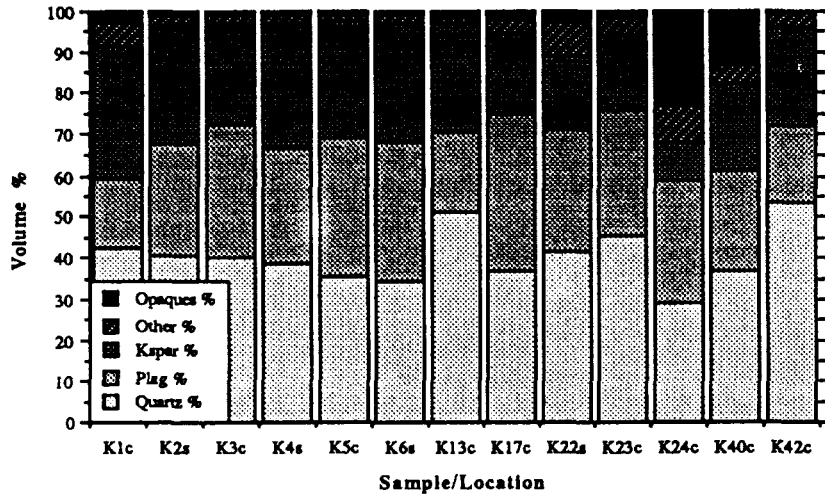
Figure 1. Mineral percentages derived from point-counts of thirteen sand samples. Sample numbers represent the collection site with a 'c' or 's' extension indicating a dune crest or swale. Samples K1c through K6s were collected from the same color unit and analyzed to verify the accuracy of the point-counting technique (note the similarity of the percentages). Samples K13c through K42c were collected along a 9.5 km N-S traverse through the most active region of the dune field (note the variation when compared to the first six samples). Also significant is the low average quartz percentage (40.4%).

2. SAMPLE ANALYSES

Forty-eight bulk samples were collected along a 9.5 km N-S traverse. These samples represented different image color units as well as position on the dune (crest vs. swale). Thirteen of the forty-eight bulk samples were chosen for detailed analyses to determine modal abundances. Six of these were from a small, mineralogically similar
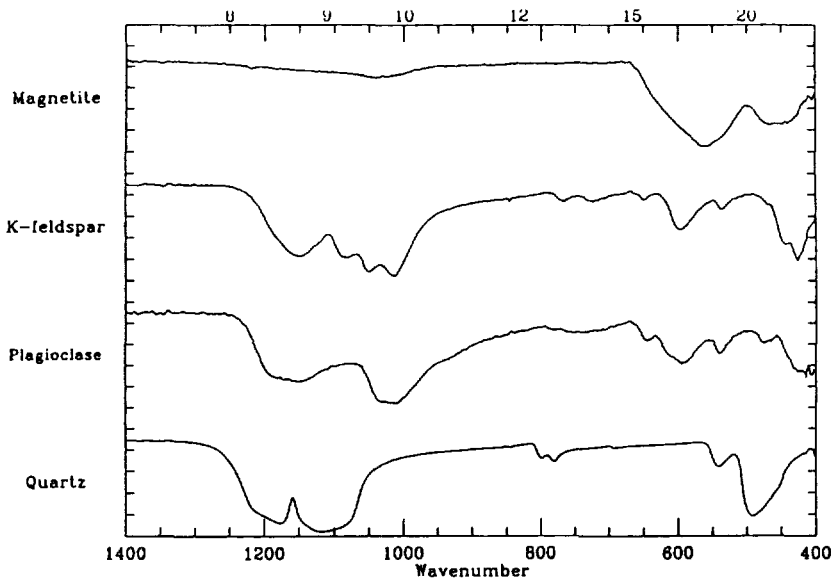
Figure 2. Laboratory emission spectra of the four endmembers - quartz, plagioclase, K-feldspar and magnetite (Avg. grain diameter = 500 - 710 μm). Minerals were separated from bulk samples using magnetic and heavy liquid separation techniques.

10

region and acted as a check on the consistency of the laboratory analysis. The bulk sand was split into 20 g samples (Cadle, 1955) from which thin sections and laboratory emission spectra were obtained (Christensen and Harrison, 1992). Over 200 grains per sample were counted to determine mineralogy and particle diameters (Jones, 1987). Samples K13c - K42c show clear mineralogic variations throughout the dune field (Fig. 1). These variations appear real based upon: *(1)* the color variations in the TIMS image; *(2)* the differences in the laboratory emission spectra; and *(3)* the similar point count results from samples K1c - K6s. Certain samples, collected from low-lying areas, contained appreciable amounts of clay. The clay component, separated from the sand using a Na-pyrophosphate dispersent, was analyzed by X-ray diffraction and found to be primarily montmorillonite. Finally, approximately 4 g of the dominant mineralogic components were separated using heavy liquid (Na polytungstate) and magnetic separation. While tedious, this separation insured the use of the correct endmembers for the dunes. Because the spectrum of plagioclase, for example, can vary dramatically as a function of An number, separation is preferred over the use of library spectra. The spectra of these endmember minerals (Fig. 2) were used as inputs into the unmixing algorithm for both the lab and image spectra.
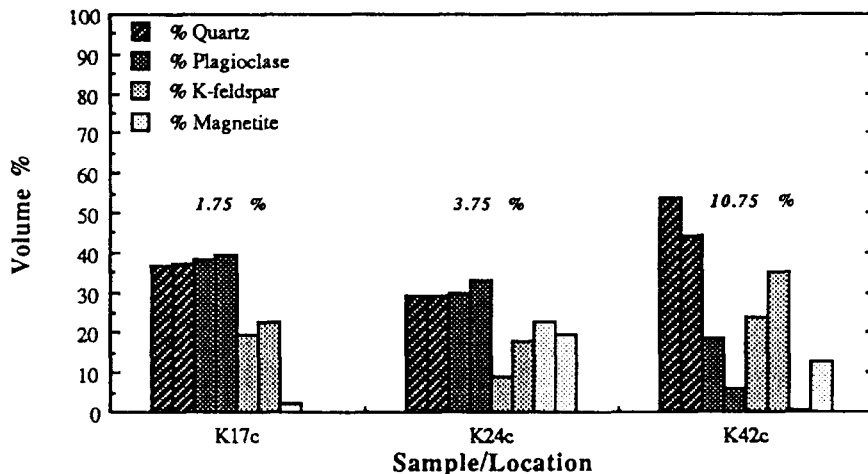
Figure 3. Comparison of endmember percentages derived from point counts (first bar) and the unmixing model (second bar). The three samples show the best, average and worst case error.

3. KELSO DUNES IMAGE ANALYSIS

Thermal Infrared Multispectral Scanner (TIMS) data for the Kelso region of the Mojave Desert were acquired in September 7, 1984. Ground resolution at nadir was approximately 17 m/pixel. The original flight line extends north from the dunes to the southernmost Cima basalt flows (Barbera, 1989). The data were calibrated and geometrically corrected for the scan angle of the instrument. Atmospheric path radiance was removed using LOWTRAN7 with the standard midlatitude summer model. The calibrated radiance images were then converted to six emissivity and one brightness temperature image (Realmuto, 1990) using a maximum assumed emissivity of 0.973 (derived from the average of all laboratory spectra). The spectra of the mineralogic endmembers convolved with the TIMS filter functions resulted in 6-point spectra that were used as inputs into the unmixing model. Mineral percentage images show very high concentrations of feldspar within the dunes as well as on alluvial surfaces extending from the immediate mountain ranges. This relation, coupled with the lack of feldspar being introduced from the previously assumed western source, indicates this mineral is

locally derived. By similar reasoning, the magnetite and other mafic minerals seem to be the direct result of weathering of amphibole rich metasediments in the Granite Mountains. While a certain percentage of the quartz within the dunes is likely derived locally, it appears, based on a higher concentration to the northwest, that some amount may come from the western source some 40 km away.

4. RESULTS

This study represents a rigorous attempt to quantify and validate the linear mixing assumption of thermal emission spectra for a real geologic surface. It also is one of the more detailed laboratory studies of the Kelso sand mineralogy. The sum of both provided an excellent validation of mineralogic retrieval algorithms to remotely acquired data. Model-derived endmembers percentages agree to within an average of 5.4% of the point count figures. The error range varied from 1.75% *(K17c)* to 10.75% *(K42c)* (Fig. 3). The general agreement between the petrographic and spectral analyses is dramatic considering the tims difference between image and sample collection, as well as the scale difference between image and lab samples. Applied to the TIMS data, the linear model reveals a much less mature dune mineralogy with a more local source for the sand than previously reported. Results of this study further the work of Ramsey and Christensen (1993) and indicate both the validity and power of the linear model especially when applied to thermal infrared image analysis.

5. REFERENCES

Barbera, P.W., 1989, *Geology of the Kelso-Baker Region, Mojave Desert, California using thermal infrared multispectral scanner data,* M.S. Thesis, Arizona State University, 198 p.

Cadle, R.D., 1955, *Particle Size Determination,* Interscience Publishers, New York, N.Y., pp. 57.

Christensen, P.R. and S.T. Harrison, 1992, "Thermal-Infrared Emission Spectroscopy of Natural Surfaces: Application to Desert Varnish Coatings on Rocks", submitted to *J. Geophys. Res.*

Gillespie, A.R., M.O. Smith, J.B. Adams and S.C. Willis, 1990, "Spectral Mixture Analysis of Multispectral Thermal Infrared Images", in *Abbott, E.A. (Ed.), Proc. of the Second TIMS Workshop, JPL Pub. 90-55,* JPL, Pasadena, Calif., pp. 57-74.

Jones, M.P., 1987, *Applied Mineralogy: A Quantitative Approach,* Graham and Trotman, Norwell, Mass., pp. 24, 74-75, 177.

Paisley, E.C.I., N. Lancaster, L.R. Gaddis, and R. Greeley, 1991, "Discrimination of Active and Inactive Sand from Remote Sensing: Kelso Dunes, Mojave Desert, California", *Remote Sens. Environ., vol. 37,* pp. 153-166.

Ramsey, M.S. and P.R. Christensen, 1992, "The Linear 'Un-mixing' of Laboratory Infrared Spectra: Implications for the Thermal Emission Spectrometer (TES) Experiment, Mars Observer", *Lunar and Planet. Sci. XXIII,* pp. 1127-1128.

Ramsey, M.S. and P.R. Christensen, 1993, "Ejecta Distribution at Meteor Crater, Arizona, Derived from Thermal Infrared Multispectral Scanner (TIMS) Data", to be submitted to *J. Geophys. Res.*

Realmuto, V.J., 1990, "Separating the Effects of Temperature and Emissivity: Emissivity Spectrum Normalization", in *Abbott, E.A. (Ed.), Proc. of the Second TIMS Workshop, JPL Pub. 90-55,* JPL, Pasadena, Calif., pp. 26-30.

Sharp, R.P., 1966, "Kelso Dunes, Mojave Desert, California", *Geol. Soc. Am. Bull., vol. 77,* pp. 1045-1074.

Yeend, W., J.C. Dohrenwend, R.S.U. Smith, R. Goldfarb, R.W. Simpson, Jr., and S.R. Munts, 1984, "Mineral Resources and Mineral Resource Potential of the Kelso Dunes Wilderness Study Area (CDCA-250), San Bernadino County, California", *U.S. Geol. Survey, Open File Report 84-647,* Washington D.C., 19 p.

REMOTE IDENTIFICATION OF A GRAVEL LADEN PLEISTOCENE RIVER BED

Douglas E. Scholen

USDA Forest Service
Southern Regional Office
Engineering Unit
1720 Peachtree Road
Atlanta, Georgia 30367

1.INTRODUCTION

The abundance of gravel deposits is as well known in certain areas across the Gulf of Mexico coastal plain, including lands within several National Forests. These Pleistocene gravels were deposited following periods of glacial buildup when ocean levels were down and the main river channels had cut deep gorges, leaving the subsidiary streams with increased gradients to reach the main channels. During the warm interglacial periods that followed each glaciation, melting ice brought heavy rainfall and torrents of runoff carrying huge sediment loads that separated into gravel banks below these steeper reaches where abraiding streams developed. As the oceans rose again, filling in the main channels, these abraiding areas were gradually flattened and covered over by progressively finer material. Older terraces were uplifted by tectonic movements associated with the Gulf Coastal Plain, and the subsequent erosional processes gradually brought the gravels closer to the surface.

The study area is located on the Kisatchie National Forest, in central Louisiana, near Alexandria. Details of the full study have been discussed elsewhere(Scholen et al., 1991). The nearest source of chert is in the Ouachita Mountains located to the northeast. The Ouachita River flows south, out of these mountains, and in Pleistocene times probably carried these chert gravels into the vicinity of the present day Little River Basin which lies along the eastern boundary of the NAtional Forest.

Current day drainages cross the National Forest from west to east, emptying into the Little River on the east side. However, a north-south oriented ridge of hills along the west side of the Forest appears to be a recent uplift associated with the hinge line of the Mississippi River depositional basin further to the east, and 800,000 years ago, when these gravels were first deposited during the Williana interglacial period, the streams probably flowed east to west, from the Little River basin to the Red River basin on the west side of the Forest.

Within the National Forest land north of Alexandria, along Fish Creek, and east and wast of an area known as Breezy Hill, exist several small, worked out gravel pits on privately owned blocks of land, formerly used by the state and county road departments. The pattern presented by these pits give the impression of a series of north-south drainages lacing through the Forest, probable tributaries to Fish Creek which flows south of east from the west side of the Forest to empty into the Little River. Because of this predominant north-south pattern, no consideration was given to areas between these drainages during early gravel exploration efforts.

2. IMAGE ACQUISITION

The initial imagery, obtained for the U.S. Forest Service during the predawn hours of early October in 1983 by the NASA, Stennis Space Center, Earth Resources laboratory, was acquired with the Thermal Infrared Multispectral

Scanner (TIMS) from the Lear 23 at an altitude of 12,000 meters above terrain, and provided data with 30 meter pixels and a swath width of approximately 18.7 kilometers. This time had been a particularly hot and dry period, and provided bone dry ground conditions as well as maximum outflow of heat from the earth's surface into the cool night sky. These conditions are ideal for obtaining good imagery for gravel search.

The 6 bands of data obtained from the TIMS operation are in digital format. This format provides a relative measure of the emissivity from the ground surface soil minerals at each of the 6 wave lengths within the mid-infrared range, and makes it possible to plot a spectral signature for each pixel.

3. SPECTRAL PROPERTIES

The materials properties that provide differences between spectral signatures of gravel deposits and deposits of other, finer grained materials are the energy absorption of the quartz molecule in TIMS band 3, the fraction of silt and clay in the material, and the thermal inertia of the material.

The energy absorption is caused by the stretching of the molecular bonds between the oxygen and silicon atoms that occurs in making up the SiO_2 molecule and its linkages. In order to maintain this configuration, the molecule must absorb energy from outside itself in the wave lengths associated with the TIMS band 3. This provides the striking signature associated with quartz. Gravel, and clean, dry, coarse grains provide the strongest signatures. Silt, impurities from clay minerals or other rock minerals, all tend to produce photon scattering which dilutes the signature.

The coarse nature of sand deposited with gravel deposits is a result of the velocity of flow in the channel. Finer particles resist settlement until still water is reached, preventing the fine and coarse materials from intermingling. Coarse sand and gravel settle out in moving water. This separation is assisted by lateral movements in the river channel. A river carrying a coarse grained load will develop a straight, shallow channel, but will change to a meandering, deep channel when the bedload becomes silt and clay leaving much of the coarse grained deposit intact.

The predominance of coarse sands found associated with gravel deposits identified by the TIMS gravel signatures indicates that these signatures are characteristic of coarse grained quartz deposits, and conversely, that the strong energy absorption in TIMS band 3 is maximized by coarse grained quartz. Thus a marked decrease in band 3 emission (and correspondingly greater dip in the signature at this point) can be expected for the coarser sized sands and gravels, as compared to the finer grained silts.

4. THERMAL INERTIA

The thermal inertia of materials provides for striking contrasts in surface temperatures. Thermal inertia expresses the resistance of a material to temperature change. Materials of high thermal inertia change temperature only very slowly, lagging behind changes in adjacent materials with low thermal inertia. A deposit of sand and gravel for example has a higher thermal inertia than a deposit of sand. This difference is most apparent in TIMS band 3, at 9.3 microns wavelength due to the energy absorption by Si-O molecular bonding, which maintains a low temperature at this wavelength while the sandy gravel mass absorbs heat from solar radiation.

The combination of maximum summer heating together with early morning cooling provides for a unique effect associated with materials of high thermal inertia. The temperature rises high in the low thermal inertia sand exposed over the summer months to the hot sun warming the surface. The higher thermal inertia gravel absorbs more heat than the sand but resists temperature change, warming more slowly, and in the predawn hours of early Fall, surface cooling

produces a lower surface temperature over the gravel body than over the sand deposits, when viewed in TIMS band 3. Gravel/sand deposits always show cooler in the TIMS band 3 imagery than adjacent nongravel/sand deposits, although warmer than the damp bottom land.

5. IMAGE PROCESSING

Imagery is processed on a 486 PC with 650MB hard drive and 90 MB Bernouli, using ERDAS 7.5 software and ARCINFO. The image for this study was pepared from the 1983 TIMS imagery. A subset including the area of concern was corrected to uniform pixel size by multiplying raw DN's by the Cos ^{4} of the angle from Nadir. The scene was rectified and georeferenced, and a road map from the GIS file was superimposed to assist in the geographic location of gravel signature. Bands 2,3 and 4 were diplayed in blue, green and red respectively. The gravel signature was developed using the ERDAS SEED software. Using the cursor, single pixel seeds were located which show the maximum difference between TIMS bands 3 and 4 in the cooler areas of the scene, and these were alarmed to the entire scene. Several seed pixels were located due to the range in temperatures across the gravel deposits. The resulting gravel signature is actually a composite. Seed pixels can be located by searching along the edges of the darker areas of the image. The lower DN's on gravel deposits in band 3, caused by the greater absorption of radiation, results in a moderately dark image. While drainage bottoms are generally dark, the signature of silt is relatively flat. The brightest areas are ridge tops, unless gravel is present on the ridge to reduce the brightness. The difference between DN's in bands 3 and 4 increases with increasing brightness. An open gravel pit will have a very large increase from band 3 to band 4.

6. DISCOVERY

During the image processing procedure associated with gravel deposit search, blocks of imagery are processed and studied for potential gravel signature. The area on the east side of the Forest, directly south of Fish Creek, was found to be obscured by clouds which formed during the overflight. To the north of this cloud cover, the processed raw image data indicated gravel signature in a nearly uniform east-west band, that appeared to be some kind of data anomaly. Initially, no attention was given to it. Subsequently, the image in this area was rectified to map coordinates, and it was discovered that the band of gravel signature actually trends north of west across the Forest for over 14 kilometers, and crosses the Fish Creek drainage at a narrow angle near the mid point of the signature band. The signature band thus runs nearly at 90 degrees to the north-south tributaries to Fish Creek, and crosses a number of low north-south trending ridges lying between these tributary drainages.

Several of these ridges were already accessible to our drill rig on existing road tracks. On each of these where drilling was performed, shallow gravel deposits were found in the area where the gravel signature crossed the ridge. Following these successes, other less accessible ridges were accessed through brush, or by bulldozing a temporary access through light timber. In each of these areas investigated, gravel deposits were found in the locations indicated by the imagery, and work continues as other ridges become accessible. Thickness of the deposits varied from a meter up to nearly 10 meters. Overburden varied from 0 to 2 meters. Total volume of gravel in these deposits is estimated to exceed 500,000 cubic meters. The width of the 8 kilometer gravel run probably averages 60 meters, providing an indication of the size of the ancient river bed.

7. REFERENCES

Scholen, D.E., W.H. Clerke, and G.S. Burns, "Remote Spectral Identification of Surface Aggregates by Thermal Imaging Techniques: Progress Report". In International Society of Optical Engineers (SPIE), Vol. 1492 Earth and Atmospheric Remote Sensing, pp 359-369, 1991.
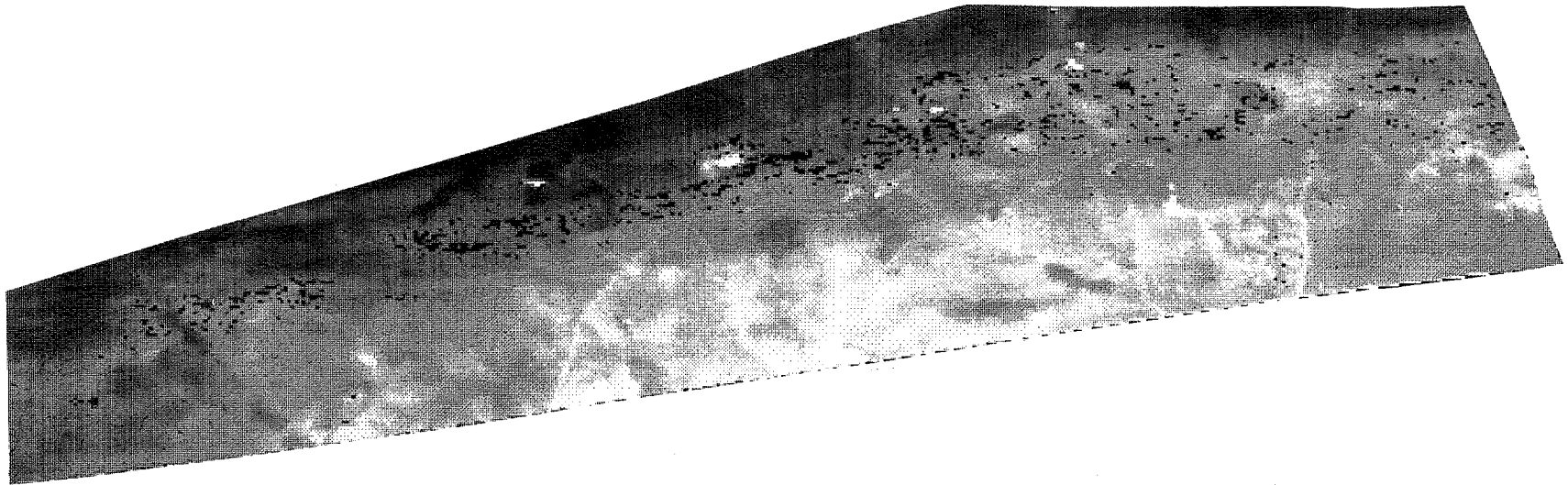
Figure 1. TIMS 30 meter resolution image of the Breezy Hill area, Catahoula Ranger District, Kisatchie National Forest. The image has been partially rectified, and processed to highlight pixels with a quartz gravel signature, indicated by the pattern of black spots spread across the image. The gravel deposits lie on flat, current day ridges, along the former channel of a meandering, Pleistocene Age, river. The bright curved line extending from mid lower image to the upper right is Grant Parish Road 123. The bright north-south line at the right is US165, north of Alexandria, LA. The large bright spot near image center is a pond in the Fish Creek drainage, which crosses the parish road and flows slightly south of east, through the bright area. Fish Creek to the west is obscured by clouds.

1. Report No. 93-26, vol. 2	2. Government Accession No.	3. Recipient's Catalog No.
4. Title and Subtitle Summaries of the Fourth Annual JPL Airborne Geoscience Workshop, October 25-29, 1993 Volume 2. TIMS Workshop		5. Report Date October 25, 1993
		6. Performing Organization Code
7. Author(s) Vincent J. Realmuto, editor		8. Performing Organization Report No.
9. Performing Organization Name and Address JET PROPULSION LABORATORY California Institute of Technology 4800 Oak Grove Drive Pasadena, California 91109		10. Work Unit No.
		11. Contract or Grant No. NAS7-918
		13. Type of Report and Period Covered JPL Publication
12. Sponsoring Agency Name and Address NATIONAL AERONAUTICS AND SPACE ADMINISTRATION Washington, D.C. 20546		
		14. Sponsoring Agency Code RF4 BP-465-66-00-01-00

15. Supplementary Notes

16. Abstract

This publication contains the summaries for the Fourth Annual JPL Airborne Geoscience Workshop, held in Washington, D.C. on October 25-29, 1993. The main workshop is divided into three smaller workshops as follows:

- o The Airborne Visible/Infrared Imaging Spectrometer (AVIRIS) workshop, on October 25-26. The summaries for this workshop appear in Volume 1.
- o The Thermal Infrared Multispectral Scanner (TIMS) workshop, on October 27. The summaries for this workshop appear in Volume 2.
- o The Airborne Synthetic Aperture Radar (AIRSAR) workshop, on October 28-29. The summaries for this workshop appear in Volume 3.

17. Key Words (Selected by Author(s)) Environmental biology Instrumentation and photography Geology and mineralogy Snow, ice, permafrost	18. Distribution Statement Unclassified; unlimited	
19. Security Classif. (of this report) Unclassified	20. Security Classif. (of this page) Unclassified	21. No. of Pages 28	22. Price